BNL-229300-2025-JAAM

Bonding and reactivity of isostructural uranyl and neptunyl peroxide phases

H. Rajapaksha, S. E. Mason

To be published in "Communications Chemistry"

November 2025

Center for Functional Nanomaterials

Brookhaven National Laboratory

U.S. Department of Energy

USDOE Office of Science (SC), Basic Energy Sciences (BES). Scientific User Facilities (SUF)

DISCLAIMER

Bonding and Reactivity of Isostructural Uranyl and Neptunyl Peroxide Phases

Harindu Rajapaksha[a], Grant C. Benthin[a], Emma L. Markun[a] , Cameron J. Flester[a] , Sara E. Mason*[a,b], Tori Z. Forbes*[a]

[a] *Department of Chemistry, University of Iowa, Iowa City, IA 52242, USA*
[b]*Center for Functional Nanomaterials, Brookhaven National Laboratory, Upton, NY 11973, USA*

*Corresponding Authors: Tori Z. Forbes Email: tori-forbes@uiowa.edu, Sara E. Mason Email: smason@bnl.gov

Abstract

Understanding the reactivity of actinide peroxide complexes is critical for predicting the behavior of spent nuclear fuel in radiolytic environments. Herein, we report the synthesis and characterization of a novel lithium neptunyl(VI) hydroxo peroxo phase (**LiNp**), which is isostructural to the uranyl analogue (**LiU**). Single-crystal X-ray diffraction reveals that **LiNp** contains both $[NpO_2(O_2)_3]^{4-}$ and $[NpO_2(OH)_4]^{2-}$ units stabilized by Li^+ and hydrogen bonding and Raman spectroscopy shows systematic redshifts in neptunyl vibrational modes relative to uranyl. DFT calculations highlight the importance of secondary coordination in reproducing vibrational and structural features, but challenges remain with correctly modeling strong sigma donors. Solid-state EPR spectroscopy and DFT confirm superoxide stabilization within **LiU** and calculations suggest favorability of the analogous radical species in **LiNp**. Solution state EPR spectroscopy with the radical spin trap 5-tert-butoxycarbonyl-5-methyl-1-pyrroline N-oxide (BMPO) reveal evidence of superoxide in the **LiU** and **LiNp** phases and suggests stabilization of superoxide within actinyl triperoxide complexes, forming $[AnO_2(O_2)_2(O)_2^*]^{3-}$.

Introduction

High ionizing radiation fields produced from nuclear materials can lead to the formation of free radicals and reactive species that further complicate the already complex chemical processes in the nuclear fuel cycle. Within aqueous solutions, ionizing radiation will generate water radiolysis products, including $e^-_{(aq)}$, $H^*_{(aq)}$, $OH^*_{(aq)}$, peroxides ($H_2O_{2(aq)}$, $HO^-_{2(aq)}$, $O^{2-}_{2(aq)}$), and superoxide ($HO^*_{2(aq)}$, $O^{*-}_{2(aq)}$) species.[1-4] These reactive ions and molecules can impact the nuclear fuel cycle processes by corroding UO_2 fuel pellets,[5,6] degrading organic extractants used in radiological separation,[7] and promoting the formation of secondary alteration products on the surface of nuclear waste forms.[8-10] These alteration phases increase the risks of storing and handling spent nuclear fuel by forming more reactive actinide-bearing compounds.[11,12]

Among the reactive species produced by water radiolysis, the peroxide anion (O_2^{2-}) is the most relevant for chemical timescales and has been previously identified as an important species throughout the fuel cycle. Peroxide is added as an oxidant during the milling process and U(VI) peroxides are often a starting material for the production of yellow cake.[13,14] On the back end of the fuel cycle, U(VI) peroxides, studtite ($[(UO_2O_2(H_2O)_2] \cdot 2\ H_2O$) and meta-studtite ($[(UO_2O_2(H_2O)_2]$), have been identified as corrosion products formed on the surface of nuclear fuel under aqueous conditions.[15-17] In addition, reprocessing schemes, such as the CARBEX process rely on the formation of peroxo and peroxocarbonate species under alkaline conditions for oxidative dissolution of the uranium solids.[18] Under these conditions, a range of actinide species are predicted to form including coordination complexes ($[AnO_2(O_2)_3]^{4-}$) and larger peroxo clusters.[19-21]

While much of the research on actinide peroxide chemistry has focused on uranium, it is equally important to understand the behavior of other actinides, particularly Neptunium-237 (^{237}Np) in similar oxidative environments.^{237}Np a minor actinide generated in nuclear reactors primarily through two pathways: (1) $^{238}_{92}\mathrm{U}(\mathrm{n},2\mathrm{n})^{237}_{92}\mathrm{U} \rightarrow {}^{237}_{93}\mathrm{Np} + {}^{0}_{-1}\beta + \bar{\nu}_e$ and (2) $^{235}_{92}\mathrm{U}(\mathrm{n},\gamma)^{236}_{92}\mathrm{U}(\mathrm{n},\gamma)^{237}_{92}\mathrm{U} \rightarrow {}^{237}_{93}\mathrm{Np} + {}^{0}_{-1}\beta + \bar{\nu}_e$. Due to its long half-life (~2.14 × 10^6 years), ^{37}Np is a significant contributor to the long-term radiotoxicity of spent nuclear fuel and nuclear waste.[22-25] It is also used as a precursor to produce ^{238}Pu, a radionuclide widely used in radioisotope thermoelectric generators (RTGs) for space missions.[26] Despite its significance, the coordination chemistry of neptunyl species under oxidizing conditions, particularly in the presence of water radiolysis products such as peroxide remains poorly understood.

To date, only two neptunyl peroxide compounds have been structurally characterized. The first, synthesized by Burns *et al.* in 2005, was a nanocluster (Np-24) with the composition $Li_{20}[Li_6(H_2O)_8NpO_2(H_2O)_4(NpO_2(O_2)(OH))_{24}]$ that was isolated from a solution containing H_2O_2 and LiOH.[27] The Np-24 nanocluster is composed of neptunyl hydroxoperoxo complexes linked together to form a sphere containing 24 Np(VI) cations. An additional $[NpO_2(H_2O)_4]^{2+}$ moiety was reported to exist in the center of the Np-24 nanocluster, but the observed bond lengths and geometry suggest it could alternatively be identified as a $[NpO_2(OH)_4]^{3-/2-}$ unit.[28] The second known neptunyl peroxide compound was isolated by Hickam *et al.* in 2019 and contains isolated units of $[NpO_2(O_2)_3]^{4-}$ charged balanced by Ca^{2+} cations.[29] Raman spectroscopy was also collected for the $Ca_2[NpO_2(O_2)_3]\cdot 9\ H_2O$ phase and included several features between 600-750 and 800-850 cm^{-1} that corresponded to neptunyl and peroxide vibrational modes, respectively. To date, there are no structurally characterized Np(IV) or Np(V) peroxide compounds. In contrast, few peroxide compounds of Th(IV) and Pu(IV) have been reported. A detailed discussion of those systems is

beyond the scope of this study, and we encourage readers to refer to the review by Kruse *et al*[30]. for further information. While these two studies provided a structural basis for the Np(VI) peroxide coordination complexes, there is still limited information on the overall chemistry of this system. This highlights a critical need to explore the chemistry of neptunyl peroxides, giving special attention to their chemical reactivity.

Herein, we report the synthesis and isolation of a novel lithium neptunyl hydroxo peroxo phase (**LiNp**), which is isostructural to its uranyl analogue (**LiU**),[31] providing a unique platform for comparing structure, bonding, vibrational modes, and reactivity. The structure of **LiNp** was determined by single-crystal X-ray diffraction and Raman spectroscopy, supported by Density Functional Theory (DFT) calculations, was used to probe the vibrational features and bonding in both phases. Solid-state Electron Paramagnetic Resonance (EPR) spectroscopy was performed to investigate the reactivity of peroxide to form oxygen-centered radicals in **LiU**. Additionally, solution-state EPR spectroscopy with 5-tert-butoxycarbonyl-5-methyl-1-pyrroline N-oxide (BMPO) spin traps were used to further investigate the presence of radioactive oxygen species within **LiU** and **LiNp**.

Results and Discussion

Characterization of the Np(VI) peroxide solid

When the Np(VI) stock solution was added to a mixture of LiOH and H_2O_2, the color changed from light red to deep dark red, indicating that peroxide likely formed a complex with the Np(VI) ion. While the Np(VI) stock solution contains features in the NIR region (1226 nm, Supporting information (SI) Section 2.1, Figure S5), the UV/Vis/NIR spectrum of the Np(VI) peroxide solution in LiOH only displays a weak, broad feature centered at 600 nm (SI Section

2.1,Figure S5). The Raman spectrum of the solution exhibits multiple features characteristic of peroxide species, including an intense band at 850 cm^{-1} attributed to the free OOH^- (SI Section 2.1, Figure S5 d). The high pH of the final solution (>12) promotes deprotonation of hydrogen peroxide (pK_a= 11.6), facilitating the formation of OOH^-. To confirm this assignment, a reference Raman measurement of H_2O_2 in 2 M KOH was performed, which exhibited a peak at 848 cm^{-1}, This is within instrumental error of the observed value and supports the assignment of the 850 cm^{-1} band to free OOH^- (SI Section 5, Figure S22). Additionally, a weaker band at 815 cm^{-1} is consistent with the presence of peroxide (O_2^{2-}) coordinated to the Np(VI) center. The feature at 704 cm^{-1} can be assigned to the symmetric stretching vibration of the neptunyl unit in the $[NpO_2(O_2)_3]^{4-}$ complex and is supported by solid-state data (Table 2). The band at 666 cm^{-1} falls within the expected range for the symmetric stretching mode of neptunyl in neptunate(VI) compounds, which are known to form under highly alkaline conditions. Additionally, the presence of multiple bands in the 500-300 cm^{-1} (SI Section 2.1, Figure S5 d)region further supports the formation of neptunate(VI) species, as these compounds typically exhibit several Raman-active modes in this spectral range.[32]

Upon addition of methanol as a crystallization agent, large (100 μm), blocky crystals (**LiNp**) with good yields (Fig. 1a) were obtained and structurally characterized using single-crystal X-ray diffraction. The compound crystallizes in a cubic *Pm*-3*m* space group and the unit cell contains twelve $[NpO_2(O_2)_3]^{4-}$ and three $[NpO_2(OH)_4]^{2-}$ units, with overall charge-balancing achieved by the presence of Li^+ cations (Fig. 1b). The Np=O bond length within the $[NpO_2(OH)_4]^{2-}$ moiety (1.79(1) Å) fit with the expected value reported by Clarke *et al*., whereas the neptunyl bond distance observed in the $[NpO_2(O_2)_3]^{4-}$ complex is longer (1.834(4) Å), but consistent with previously reported neptunyl triperoxide complex (1.843(7) Å).[21,29,33] This bond elongation likely results from significant electron donation from the peroxide ligands to the actinyl center, which

increases the Lewis basicity of the axial oxygen atoms, enhancing their ability to engage in actinyl–cation interactions .[34,35] In the crystal structure, each axial oxygen in $[NpO_2(O_2)_3]^{4-}$ interacts with three Li^+ ions, with average Li–O distances of 2.266 Å and each Np(VI) triperoxide complex is surrounded by twelve water molecules hydrogen-bonded to the peroxide ligands. Additional water molecules are located within the interstitial regions to give an overall formula of $(Li_{18}[NpO_2(O_2)_3]_4[NpO_2(OH)_4]\cdot 39.5\ H_2O)$.

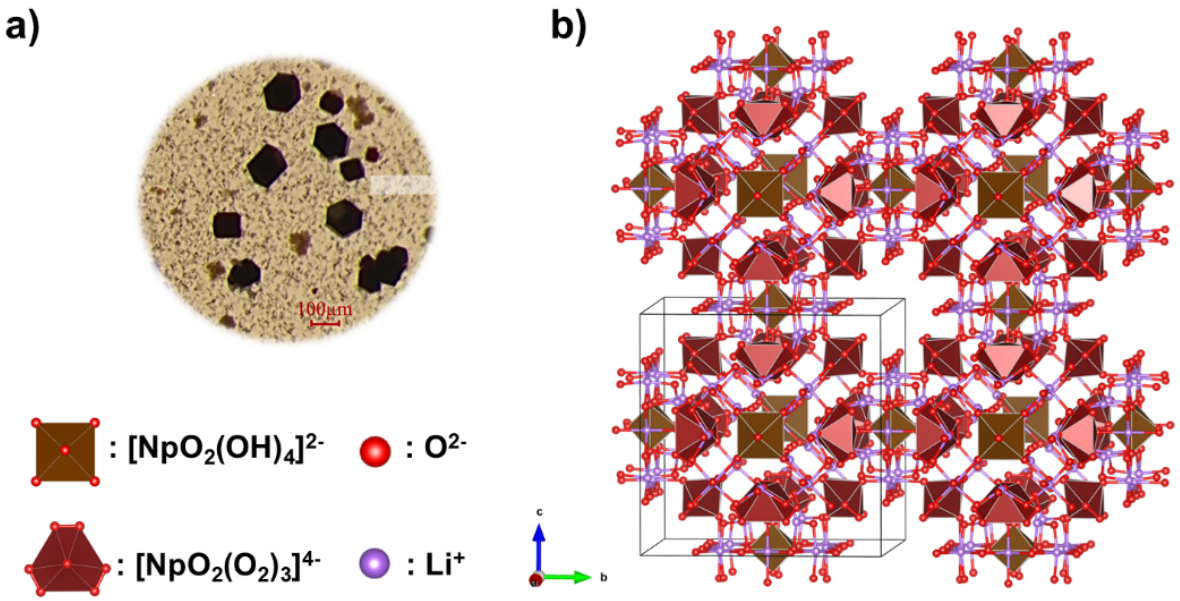

Figure 1: **a)** Optical microscope image of the product shows the formation of a blocky, dark-red crystalline phase (**LiNp**). **b)** Structural characterization of **LiNp** indicates that the material is composed of $[NpO_2(O_2)_3]^{4-}$ and $[NpO_2(OH)_4]^{2-}$ coordination complexes that are charge-balanced with Li^+ cations.

The **LiNp** phase is isostructural to a uranyl peroxo hydroxo phase previously reported by the Nyman group (Table 1).[31] While the bond distances observed in the $[AnO_2(OH)_4]^{2-}$ units are consistent with expected changes, subtle differences can be observed for the $[AnO_2(O_2)_3]^{4-}$ complex. The NpO_2^{2+} cation has one additional electron compared to UO_2^{2+}, which occupies a non-bonding *f* orbital on the actinyl center. This added electron can repel the negatively charged axial oxo ligands, and as a result, Np(VI)=O bond lengths are generally expected to be longer than

the corresponding U(VI)=O bonds. However, in the $[AnO_2(O_2)_3]^{4-}$ unit of **LiNp**, the Np(VI)=O bond is observed to be 0.016 Å shorter than the U(VI)=O bond in the analogous **LiU** complex. The An-O equatorial distances are within error, but the peroxo bonds in the Np(VI) compound is 0.034 Å shorter than the distance observed in the U(VI) compound. We also note that one of the Li^+ cation interactions to the neptunyl oxo atoms is slightly longer than what is observed in the related U(VI) compound, suggesting weaker second-sphere electrostatic interactions. However, resolving Li^+ cation positions using XRD can be challenging, particularly in a high symmetry unit cell, and may not provide an accurate assessment of the extended coordination environment.

Table 1. Summary of bond lengths (Å) and interactions distances (Å) associated with the uranyl and neptunyl hydroxo peroxo compounds.

Bond length Å		**LiU***	**LiNp**
$[AnO_2(O_2)_3]^{4-}$	An=O (actinyl)	1.850(8)	1.834(4)
	An-O_2 (actinyl peroxide)	2.281(8)	2.281(4)
		2.310(9)	2.301(4)
		2.327(9)	2.325(4)
	O-O (peroxide)	1.49(1)	1.497(6)
		1.51(2)	1.476(8)
	An=O--Li^+	2.200(8)	2.237(4)
		2.25(4)	2.28(2)
		2.25(4)	2.28(2)
$[AnO_2(OH)_4]^{2-}$	An=O (actinyl)	1.77(4)	1.79(1)
	An-OH (actinyl hydroxide)	2.29(3)	2.23(1)
	An=O--Li^+	1.93(6)	1.94(2)

* Bond distances for LiU were taken from Reference 19. Crystallographic parameters for LiNp can be found in the SI, Table S2.

To gain deeper insight into the bonding characteristics of the material, we employed Raman spectroscopy (Fig. 2). The AnO_2^{2+} cation has four fundamental vibrational modes: symmetric stretch (Raman active ν_1), doubly degenerate bending mode (IR active ν_2), and antisymmetric stretch (IR active ν_3).[36,37] Additional vibrational features can appear from ligand vibrations and AnO_2^{2+}-ligand stretching modes. Neptunyl vibrational bands generally exhibit a red shift compared to their uranyl counterparts. This shift is attributed to a weakened actinyl bond resulting from increased electron density at the neptunium center and enhanced non-covalent interactions involving the axial oxygens in neptunyl complexes.[33,38,39]

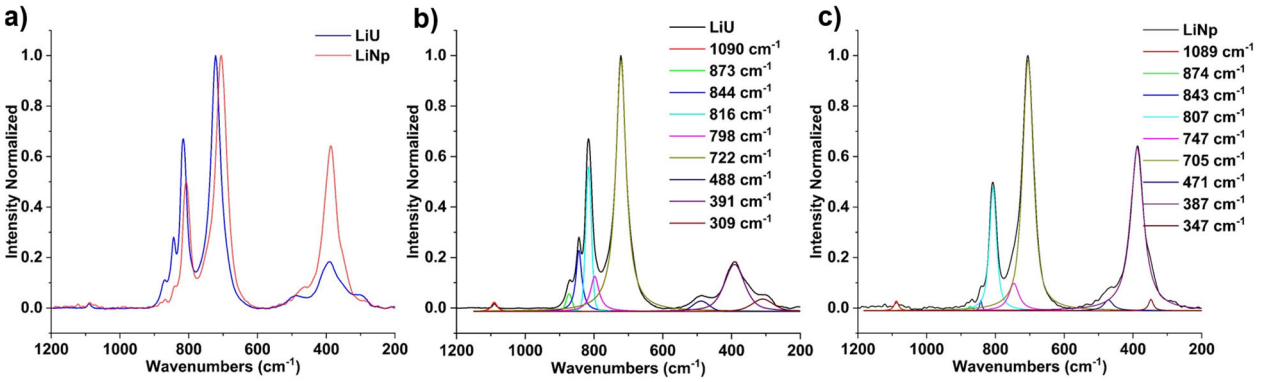

Figure 2. **a)** The stacked Raman spectra of **LiU** (blue) and **LiNp** (red) emphasize the red shift of the neptunyl peroxide bands. Peak fittings of **(b) LiU** and **(c) LiNp** solid phases provide quantitative assessment of the peak shifts between the isomorphous solids. Spectral intensities are normalized with respect to maximum intensity peak to aid in comparison between the two compounds.

For the **LiNp** phase, the neptunyl symmetric stretch (ν_1) associated with the $[NpO_2(O_2)_3]^{4-}$ complex is observed at 705 cm^{-1}, representing a redshift of 17 cm^{-1} relative to the corresponding ν_1 band of $[UO_2(O_2)_3]^{4-}$ in **LiU** (Fig. 2a and 2b, Table 2). Based on crystallographic data, one might expect the ν_1 band of $[UO_2(O_2)_3]^{4-}$ to appear at lower energy than that of the neptunyl analogue due to the longer U=O bond length (1.850 Å)[31] compared to Np=O (1.834 Å). This trend is also observed for the $Ca_2[AnO_2(O_2)_3]$ system as the An=O bond distances are within error, but the Raman-active Np=O ν_1 band is 20 cm^{-1} red-shifted compared to the U(VI) analogue.[21,29] These

discrepancies highlight that crystallographic data alone are insufficient for reliably predicting vibrational band within actinyl solids, particularly for peroxide complexes.[38]

Table 2. Summary of the LiU and LiNp solid-state Raman peak assignments

LiU Peak centroids (cm^{-1})	LiNp Peak centroids (cm^{-1})	Peak Shift (LiU-LiNp) (cm^{-1})	Peak assignment
1090	1089	1	CO_3^{2-} symmetrical stretching of the C-O bond
873	874	-1	Actinyl cation coordinated O_2^{2-} in-phase symmetrical stretching (ν_1)
844, and 816	843, and 807	1, and 9	Actinyl cation coordinated O_2^{2-} out-of-phase symmetrical stretching ($\nu_2$and ν_3)
798	747	51	$[AnO_2(OH)_4]^{2-}$ actinyl cation symmetrical stretching (ν_1)
722	705	17	$[AnO_2(O_2)_3]^{4-}$ actinyl cation symmetrical stretching (ν_1)
488,391,and 309	471, 387, and 347	17, 4, and -38	AnO_2^{2+}- O_2^{2-} stretching modes

Other features present in the Raman spectra match well with previously reported compounds. Vibrational modes located at 798 and 747 cm^{-1} in the **LiU** and **LiNp** spectra, respectively, can be linked to the $[AnO_2(OH)_4]^{2-}$ complex as Clark *et al.* previously reported uranyl and neptunyl symmetric stretching vibrations for these species at 796 and 741 cm^{-1}, respectively.[28,40] Vibrational bands of peroxide bound to actinyl cation are observed at 873–874 cm^{-1} (ν_1), 843–844 cm^{-1} (ν_3), and 807–816 cm^{-1} (ν_2) and they match well with literature values.[21,29] Additional peaks in the 300–600 cm^{-1} range can be attributed to AnO_2^{2+}-peroxide stretching modes based upon previous work by Margate *et al.*[41] A weak feature at 1089–1090 cm^{-1} present in both spectra is attributed to residual carbonate on the surface of the crystals, potentially formed from the reaction between CO_2 and hydroxide. This reaction can occur either in the LiOH stock solution or during the crystal isolation from motherliquor.

DFT calculations were utilized to further confirm the Raman-active vibrational modes and bond distances (SI, Tables S4 and S5). Significant discrepancies were observed between the calculated and experimental results, consistent with similar findings previously reported by others.[21,29] It is important to note that the theoretical vibrational frequency calculations presented here are based on the harmonic oscillator approximation; therefore, some discrepancy between experiment and theory is expected. However, previous DFT studies on Raman features of other molecular actinyl systems (eg: $[NpO_2Cl_4]^{2-}$) have demonstrated greater agreement with experimental data compared to the triperoxide unit discussed in this work.[34,42,43]

For the $[AnO_2(O_2)_3]^{4-}$ unit, calculations using the bare actinyl–peroxide complex (Model I) overestimate the bond distances by 0.04-0.05 Å and underestimate the actinyl ν_1 band by 76 and 50 cm^{-1} for U and Np, respectively. Prior work noted the importance of the second coordination sphere to correctly predict the band positions,[38,39] so we developed three additional models for the $[AnO_2(O_2)_3]^{4-}$ unit and one for the $[AnO_2(OH)_4]^{2-}$ species, each including explicit water molecules and Li^+ cations. When two Li^+ cations, each engaged in actinyl-cation interactions, are included in the calculations (Model II) and we find significant improvements in experimental agreement to the ν_1 actinyl symmetric stretch, reducing the discrepancies to 5 and 7 cm^{-1} for $U(VI)O_2^{2+}$ and $Np(VI)O_2^{2+}$, respectively. However, the opposite trend is observed for the peroxide vibrational modes within these systems. Model I yields lower absolute average errors of 8 and 19 cm^{-1} for the ν_1 O_2^{2-} stretching mode in the U(VI) and Np(VI) compounds, respectively, while the inclusion of secondary interactions in Model II increases these errors to 44 and 40 cm^{-1}. For bare $[UO_2(OH)_4]^{2-}$ and $[NpO_2(OH)_4]^{2-}$ complexes, the calculated actinyl ν_1 bands are underestimated by 32 and 12 cm^{-1}, and An=O bond distances are overestimated by 0.07 and 0.02 Å, respectively. Adding the second coordination sphere improves the U=O bond substantially, but the calculated actinyl ν_1

bands are now overestimated by 63 cm^{-1}. For $[NpO_2(OH)_4]^{2-}$, inclusion of the second coordination sphere leads to underestimation of the Np=O bond by 0.04 Å and overestimation of the ν_1 mode by 108 cm^{-1}.

To further investigate these discrepancies in actinyl bonding, QTAIM [49] analysis was performed at the Bond Critical Points (BCPs). The electron density at the BCP of the Np=O bonds in both the $[AnO_2(O_2)_3]^{4-}$, and $[AnO_2(OH)_4]^{2-}$ was found to be higher than that of the corresponding U=O bonds (SI Section 6.5 Table S8 and S9), suggesting a stronger neptunyl bond. However, this finding appears inconsistent with the Raman spectroscopic data, which indicates a weaker Np=O bond. This highlights the challenges in reconciling localized, equilibrium electron density descriptors with vibrational observables. Specifically, QTAIM analysis reflects the ground-state electron density at the equilibrium geometry and does not account for dynamic changes in charge distribution induced by nuclear motion. Vibrational modes can perturb the electronic structure in ways that alter bond strengths or polarizabilities, effects that may not be captured in static, topological analyses of the electron density.

To confirm that we had chosen the best methodology for the peroxide system, we benchmarked 22 density functionals for geometry optimization and vibrational frequency calculations of the of $[NpO_2(O_2)_3]^{4-}$ unit (SI, Section 1.6, Figures S1–S4). The results indicate that no single functional accurately reproduces both the experimental structural parameters of the NpO_2^{2+} core and the peroxide ligands simultaneously. Functionals such as TPSS0[44] and ωr2SCAN[45] provide highly accurate results for the actinyl cation, whereas functionals like TPSS[46] and RPBE[47] yield better agreement with the experimental data for the peroxide ligands. These results suggest that the overall limitations of DFT in this context may not stem solely from the omission of secondary coordination effects, rather from an overestimation of the sigma bond

strength in these strong donors. For the $[AnO_2(O_2)_3]^{4-}$, DFT may overestimate the An–peroxide bond strength, which in turn leads to an overestimation of electron density at the metal center and an artificial weakening of the actinyl bond.[33,48] The interplay of DFT delocalization error and the strong σ-donor character of peroxide ligands manifests in the difficulty describing mixed bonding regimes within a single functional framework. Systematic benchmarking against experimental structural and spectroscopic data provides essential feedback to guide and support the need to develop more accurate and transferable methods for complex actinide systems.

Actinyl Peroxide Radical Chemistry

Peroxide is considered part of the family of reactive oxygen species and can readily oxidize or degrade to form radical species. Previous work by Scherrer *et al.* demonstrated that over the course of several days, the U(VI) peroxide solid $K_4[UO_2(O_2)_3]$ dissolved in water would react to form U(VI) superoxide species.[50] This was also shown to occur in the solid state by both Scherrer *et al*.[50,51] and Kravchuk *et al*[11]*.,* where EPR spectroscopy confirmed the presence of superoxide in U(VI) peroxide compounds. No reactivity studies have been conducted for the Np(VI) peroxide phases; thus, we utilized EPR spectroscopy and DFT calculations for both the **LiU** and **LiNp** systems to provide additional information on their chemical behavior.

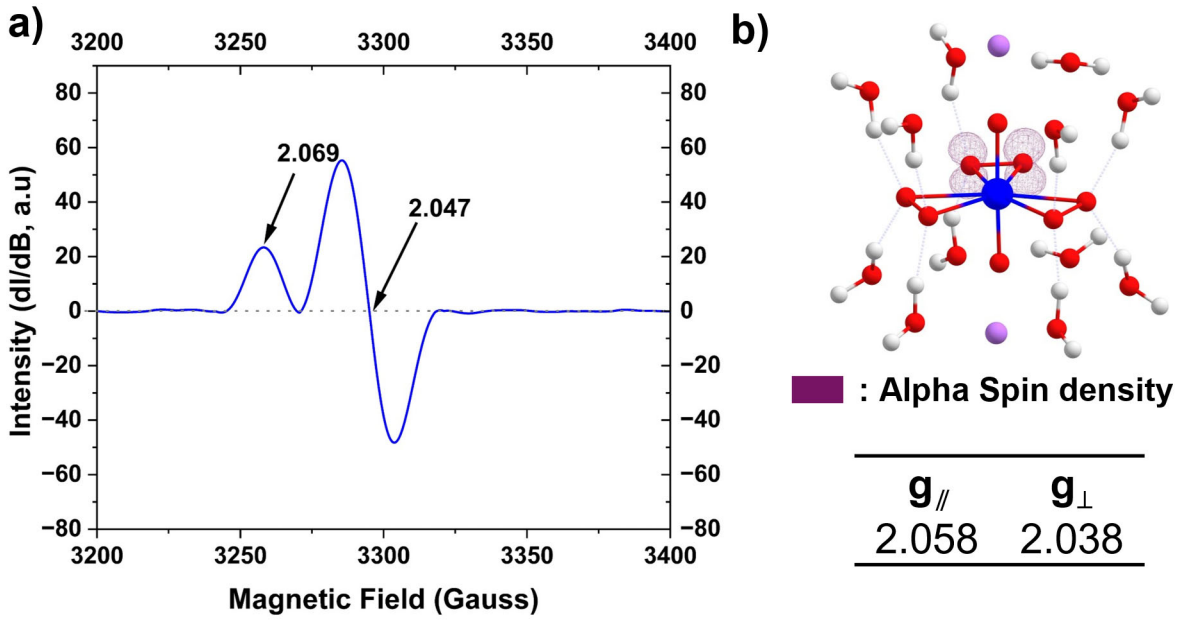

Figure 3. **a)** Solid-state EPR spectrum of the uranyl phase at room temperature and **b)** spin-density showing the formation of superoxide within $[UO_2(O_2)_2(O)_2^*]^{3-}$ unit. The spin-density is generated with iso value of 0.015. Blue, red, purple and white sphere represents U, O, Li and H respectively.

EPR spectroscopy was first used to evaluate the presence of superoxide or hydroxyl radicals in the U(VI) solid-state material. Solid-state EPR spectra of the **LiU** compound exhibited an axial signal with $g_{\|} = 2.069$ and $g_{\perp} = 2.047$ (Fig. 3a). In the solid state, superoxide commonly exhibits an axial EPR signature ($g_z \neq g_x = g_y$), with reported $g_{\|}$ values ranging from 2.034 to 2.168 and $g_{\perp}$ values from 2.005 to 2.075.[52-55] In previous work by Forbes group, we measured $g_{\|}$ and $g_{\perp}$ values for superoxide coordinated to a uranyl cation at 2.035–2.050 and 2.015–2.017, respectively.[50,51] The g-value for the unpaired electron within an atomic or molecular orbital typically deviates from the free electron (2.0023)[56] due to factors such as spin–orbit coupling, hyperfine interactions, and orbital interactions.[57,58,] It is also highly sensitive to the electronic structure and local environment of the radical species and can be influenced by secondary interactions such as hydrogen bonding and cation interaction, making it characteristic of both the chemical species and its surrounding matrix.[59-61] This is clearly observed for **LiU**, which exhibits

a shift in the EPR signal to higher magnetic field compared to the previously observed signals in the related potassium U(VI) complex.

DFT calculations were previously used to interpret the EPR signatures of radical complexes,[50,51,62] so we utilized this methodology to determine the origin of the observed solid-state EPR features within the **LiU** solid. The crystal structure contains U(VI) peroxide and hydroxide complexes, suggesting the potential presence of either a superoxide or hydroxyl radical species. Formation of these radicals requires the removal of an electron from the respective ligand ($O_2^{2-} \rightarrow O_2^{-\bullet}$ or $OH^- \rightarrow {}^{\bullet}OH$); thus, electrons were removed from the $[UO_2(O_2)_3]^{4-}$and $[UO_2(OH)_4]^{2-}$ units, generating the open-shell $[UO_2(O_2)_2(O)_2]^{3\bullet-}$ and $[UO_2(OH)_4]^{\bullet-}$ species in the simulation. For the $[UO_2(O_2)_3]^{4-}$, complex, the HOMO to HOMO-2 molecular orbitals are primarily composed of peroxide π^* character (SI, Section 6.4, Figure S25). Removal of an electron to form $O_2^{-\bullet}$ is expected to occur from these orbitals[63] and this is observed in the spin density distribution of the optimized $[UO_2(O_2)_2(O)_2^{\bullet}]^{3-}$ structure, where the unpaired spin is localized on the $2p_z$ orbitals of the two oxygen atoms within a single ligand (Fig. 3b). The calculated $g_{\parallel}$ and $g_{\perp}$ values for the bare $[UO_2(O_2)_3]^{4-}$ model (Model I) were 2.063 and 2.018, respectively. Upon inclusion of the secondary coordination sphere (Models II–IV, Supportig Information Section 5.2, Table S3), the calculated values shifted to 2.055–2.058 ($g_{\parallel}$) and 2.036–2.038 ($g_{\perp}$), bringing them into closer agreement with experimentally observed values. In contrast, the spin density of $[UO_2(OH)_4]^{\bullet-}$ is not purely ligand-centered but is delocalized across the entire molecule. This is consistent with the nature of the HOMO in $[UO_2(OH)_4]^{2-}$, which is not strictly ligand-based. The calculated g-tensor for this species is rhombic, with values of $g_x = 1.230$, $g_y = 1.629$, and $g_z = 1.986$ (SI, Section 6.2, Table S5) which significantly deviate from experimentally observed values. Furthermore, when the secondary coordination sphere was included (Model VI), the spin density localized predominantly on

surrounding water molecules, while the $[UO_2(OH)_4]^{2-}$ unit remained closed-shell (Supporting Information Section 5.4, Figure S27c). This suggests that electron removal from a water molecule in the crystalline lattice is more favorable than from the hydroxide-bound uranyl complex. Taken together, these results strongly indicate that stabilization of a hydroxyl radical in the uranyl hydroxide unit is unlikely. Instead, the species detected experimentally is best assigned as a superoxide radical coordinated within the $[UO_2(O_2)_2(O)_2^{\bullet}]^{3-}$ unit.

Solid-state EPR measurements for the solid neptunyl phase were not pursued due to radiological safety concerns. Instead, DFT calculations provided some additional insights into the system. In the $[NpO_2(O_2)_2(O)_2^{*}]^{3-}$ unit where the spin mutiplicity is three, the spin density is not confined to an equatorial ligand but is distributed between the metal center and an superoxide ligand located in the equatorial plane. Here, one unpaired electron resideing on the $2p_z$ orbital of the superoxide, while the other occupies the δ_u orbital of the neptunyl cation. The calculated g-tensor values ($g_x = 0.656$, $g_y = 1.244$, and $g_z = 1.528$, Model I) are markedly different from uranyl superoxide species. This enhancement in anisotropy and deviation from the free-electron value stems from the metal-centered unpaired electron (higher spin-orbital coupling) and the zero-field splitting intrinsic to triplet systems. Comparable shifts in g-values have been reported for actinide complexes with metal-localized spin densities.[64-67] DFT calculations also provided information on the relative stability of $[NpO_2(O_2)_2(O)_2^{*}]^{3-}$ and $[UO_2(O_2)_2(O)_2^{*}]^{3-}$ within the crystal lattice (Models II–VI) suggest that both species have similar thermodynamic stabilies with ΔG =-11.93 to 6.34 kJ/mol (SI, Section 6.2, Table S7). This result supports the idea that Np(VI) superoxide complexes could be potentially stabilized in the solid state material.

Solution-phase EPR studies are a safer alternative than solid-state measurements on dispersible powders and have previously been used to identify the presence of U(VI) superoxide

when the related potassium uranyl triperoxide phase was dissolved in water.[50] However, dissolution of the **LiU** and **LiNp** phases in water did not result in any signatures associated with the radicals in the sample (SI, Section 4.2 Figure S7 and S8). Previous work by Nienhuis *et al*. found that the identity of the alkali base affected the radical production by influencing the local solvation structures.[68] In this case, they noted that in the case of kosmotropic cations (Li^+) solvent rearrangment has a higher energy barrier, which forms a caged pair that more likely undergoes recombination. However, with chaotropic cations like K^+, there is a smaller barrier for solvent rearrangment, enabling more radical interactions and formation. This may explain the differences in superoxide radical stabilization between the previous work on K^+-containing system and the related **LiU** solution.[50]

To enhance our detection capabilities, we turned to the addition of spin traps to evaluate if short lived radicals can be observed in either the **LiU** or **LiNp** solutions. 5-tert-butoxycarbonyl-5-methyl-1-pyrroline N-oxide (BMPO) was used as a spin trap because it has been previously used for the identification of reactive oxygen species, including superoxide, hydroperoxyl, and hydroxyl radicals.[69-73] BMPO was chosen over the more common 5,5,-dimethyl-1-pyrroline-N-oxide (DMPO) spin trap due to a longer half-life of the superoxide adduct.[59] Spin traps, including BMPO, have been developed for biological systems and can be influenced by pH, radical concentrations, and presence of metal cations. In addition, high levels of radicals and redox active metals can cause degradation BMPO molecule; thus, careful control and modeling of the resulting spectra are required to fully understand the nature of the radicals in the system. These challenges will be further highlighted below.

Dissolution of approximately 5 mg of the **LiU** crystals in 200 µL of water yields a highly alkaline solution, with a pH ranging from 10 to 12 as determined by pH indicator strips. Misak *et*

al. demonstrated that under such conditions, spin trapping experiments using inorganic superoxide (KO_2) primarily produced hydroxyl radical adducts (BMPO-OH).[69] This is due to the reaction between superoxide and hydroxyl ions, which generates peroxide and hydroxyl radicals and subsequently interact with BMPO. Furthermore, **LiU** dissolved with the spin trap under highly alkaline conditions, shows the formation of paramagnetic BMPO adduct degradation product(s) at 60 minutes (SI, Section 4.3, Figure S18). However, lowering the pH beween 4-6, enables the BMPO-OOH spectra remain relatively stable over the same period. To both enhance superoxide detection and avoid formation of paramagnetic BMPO degradation products, we selected conditions that maintain a final pH between 4 and 6 for all subsequent spin-trap experiments.[69] Additionally, previous work suggested that diethylenetriaminepentaacetic acid (DTPA) should be added to chelate any trace transition metals present in the reagents, which could otherwise interfere with BMPO or its radical adducts.[74] Therefore, DTPA was also added to all of the solutions containing the BMPO spin trap. Control experiments with the uranyl or neptunyl stock and the spin trap showed no detectable EPR signal, indicating An(VI) does not generate paramagnetic products of BMPO at these experiments conditions by itself (SI, 4.3, Figure S17a-c).

Hyperfine splitting parameters of spin-traps are sensitive to matrix conditions such as ionic strength and pressence of metals.[75,76] To confirm the hyperfine parameters of BMPO-OOH and BMPO-OH adducts under experimental conditions here matched previously reported values, a control experiment was conducted using KO_2 at ion types and concentrations comparable to those expected upon dissolution of **LiU** and **LiNp**. The resulting spectra showed the hyperfine parameters were consistent with prior reports (SI, Section 4.3, Figure S11-S15) [69-71,77,78] This further supports the use of BMPO as an effective spin trap for superoxide under these experimental conditions. The validated hyperfine parameters (Table 3) were subsequently used to fit the

experimental data obtained from spin-trap experiments with **LiU** and **LiNp**. The overall process for the generation of BMPO-OOH and BMPO-OH adducts is also summarized schematically in Figure 5.

Table 3: Average g_{iso} and the hyperfine spliting parameters of messured BMPO adducts.

Adducts	g_{iso}	A_N (G)	$A_{H\beta}$ (G)	$A_{H\gamma}$ (G)
BMPO-OOH(1)	2.006	13.387	12.000	-
BMPO-OOH(2)	2.006	13.377	9.661	-
BMPO-OH(1)	2.006	13.915	15.365	0.713
BMPO-OH(2)	2.006	14.124	12.674	0.599

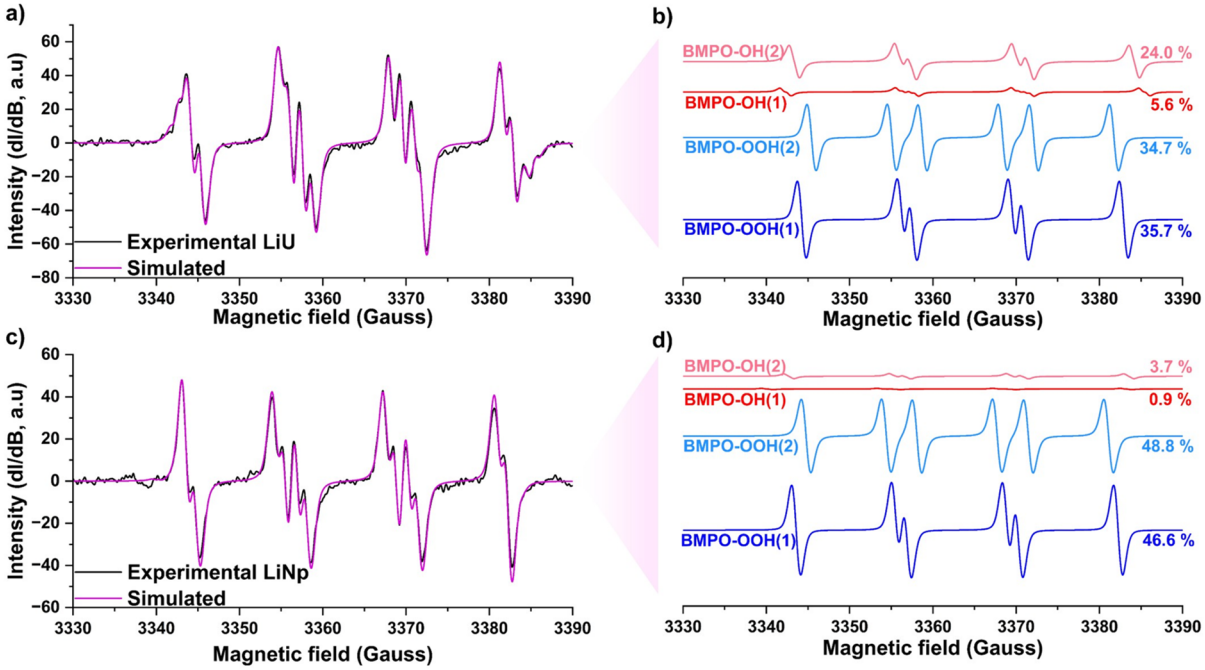

Figure 4. Solution EPR spectra of spin trap experiments with BMPO on dissolved **(a) LiU** and **(b) LiNp** with simulated fits (pink line). Each BMPO adduct associated with the fits are provided for **(c) LiU** and **(d) LiNp** with the BMPO-OH and BMPO-OOH aducts represented by red and blue lines respectively. The simulated percentages of each adduct are also provided. Additional simulated fits and experimental EPR spectra are provided in SI, Section 4.3.

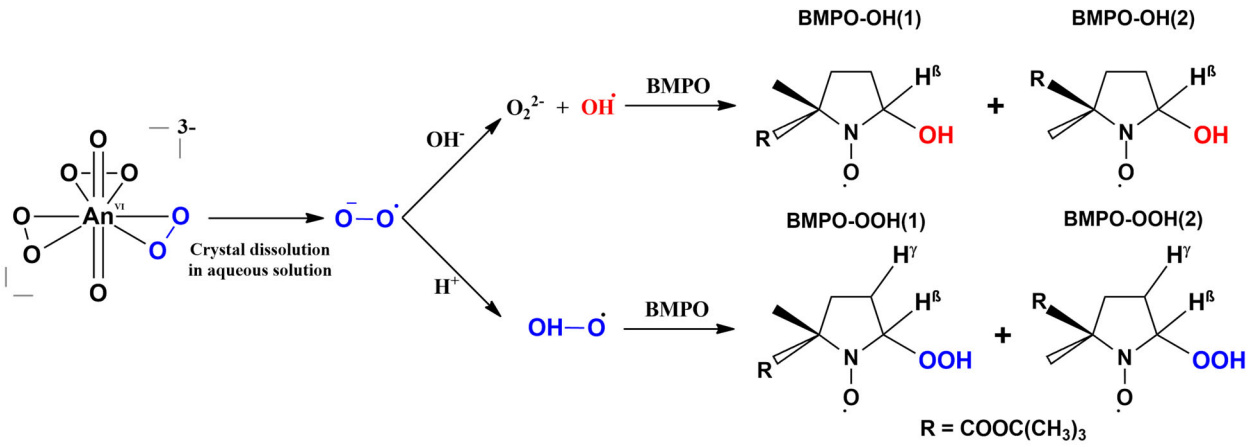

Figure 5. Schemic diagram showing the reactions involved in BMPO adducts formation starting from dissolved crystals containing superoxide complexed to actinyl cation.

The EPR spectra obtained from spin-trap experiments with **LiU** were dominated by the BMPO-OOH adduct (70.4%), with a secondary contribution from the BMPO-OH adduct (28.6%) (Fig. 4b). Similarly, spectra from the **LiNp** experiments showed a BMPO-OOH contribution exceeding 95% (Fig. 4d). To confirm that the observed signals were not the result of the reactivity of peroxide, we evaluated a control solution containing uranyl nitrate and H_2O_2 at pH 5 and found that the EPR spectra was silent (SI, 4.3, Figure S17d). These results clearly indicate that superoxide is present within the crystalline materials, supporting the stabilization of superoxide within actinyl triperoxide complexes, forming $[AnO_2(O_2)_2(O)_2^*]^{3-}$.

The presence of BMPO-OH adducts is likely due to the generation of hydroxyl radicals via the reaction of superoxide with hydroxide ions. The higher proportion of BMPO-OH observed in the **LiU** experiment may result from a higher pH (~6), while the lower percentage in the **LiNp** experiment corresponds to a lower pH (~4), which limits hydroxyl radical formation. A similar trend was observed in the KO_2 control experiments, where increasing the pH from 4 to 9 led to a

rise in the proportion of BMPO–OH and a corresponding decrease in BMPO–OOH (SI, Section 4.3, Figure S16).

Conclusion

This study reports the synthesis and characterization of a lithium neptunyl hydroxo peroxo phase (**LiNp**), which is isostructural to the uranyl analogue (**LiU**), enabling direct comparison of U(VI) and Np(VI) peroxide chemistry. Structural analysis revealed subtle differences in bonding; notably, the axial bond in the $[AnO_2(O_2)_3]^{4-}$ unit is 0.016 Å shorter in **LiNp** than in **LiU**, contrary to the typical trend. Raman spectroscopy showed consistent redshifts in actinyl vibrational modes of **LiNp** in comparison to **LiU**, while DFT calculations emphasized the critical role of the second coordination sphere for improving accuracy of the modeled actinyl vibrational and bonding features. Benchmarking across 22 functionals revealed that current DFT approaches struggle to capture both actinyl and peroxide bonding simultaneously at equal accuracy. Solid-state EPR spectroscopy and DFT calculations confirmed the presence of a coordinated superoxide radical in **LiU**. Although solid-state EPR data for **LiNp** was not collected due to radiological safety constraints, DFT results indicated the thermodynamic feasibility to have superoxide coordinated to neptunyl cation. Solution-phase spin-trapping experiments revealed direct evidence of superoxide in the both the **LiU** and **LiNp** systems, supporting the stabilization of superoxide within actinyl triperoxide complexes, forming $[AnO_2(O_2)_2(O)_2^*]^{3-}$.

Given the importance of reactive oxygen species within the nuclear fuel cycle, continued efforts are needed to fully understand the chemistry of actinide peroxide species. Future work is needed to fully understand the nature of the actinyl peroxide bonding and the challenges with the DFT calculations for these systems highlight a frontier in advancing computational modeling of actinyl complexes with stronger axial-ligand interactions. Furthermore, reactivity between free

radical species and actinide cations is important given the inherent radioactivity of these elements. Lastly, understanding chemical transformations that may occur due to the presence of reactive oxygen species is necessary to fully understand the behavior of actinides in complex aqueous solutions and predict their fate within the nuclear fuel cycle.

Supporting Information (SI): Experimental procedures and functional benchmarking, characterization of actinyl peroxide solutions, characterization of LiU and LiNp solid phases, EPR experiments including fitted spectra for spin trap experiments and control experiments, fitted Raman spectra, and DFT calculations results.

Acknowledgements

H.R, G.C.B, E.L.M, C.J.F and T.Z.F acknowledge funding support provided by the Department of Energy, Basic Energy Sciences program under DE-SC0023995. S. E. M. used the Theory and Computation facility of the Center for Functional Nanomaterials (CFN), which is a U.S. Department of Energy Office of Science User Facility, at Brookhaven National Laboratory under Contract No. DE-SC0012704. Computational support was provided in part by the University of Iowa. We gratefully acknowledge Dr. Garry R. Buettner and Brett A. Wagner from the Department of Radiation Oncology at the University of Iowa for their valuable guidance and support with spin-trapping experiments.

References

1 Sartorio, C. *et al.* Preliminary Assessment of Radiolysis for the Cooling Water System in the Rotating Target of SORGENTINA-RF. *Environments* **9**, 106 (2022).

2 Swiatla-Wojcik, D. & Buxton, G. V. Modeling of radiation spur processes in water at temperatures up to 300. degree. *The Journal of Physical Chemistry* **99**, 11464-11471 (1995).

3 Hamill, W. H. Model for the radiolysis of water. *The Journal of Physical Chemistry* **73**, 1341-1347 (1969). https://doi.org:10.1021/j100725a027

4 LaVerne, J. A. & Schuler, R. H. Production of hydroperoxo (HO2.cntdot.) in the track of high-energy carbon ions. *The Journal of Physical Chemistry* **89**, 4171-4173 (1985). https://doi.org:10.1021/j100266a005

5 Sunder, S., Miller, N. H. & Shoesmith, D. W. Corrosion of uranium dioxide in hydrogen peroxide solutions. *Corrosion Science* **46**, 1095-1111 (2004). https://doi.org:https://doi.org/10.1016/j.corsci.2003.09.005

6 Olsson, D., Li, J. & Jonsson, M. Kinetic Effects of H2O2 Speciation on the Overall Peroxide Consumption at UO2–Water Interfaces. *ACS Omega* **7**, 15929-15935 (2022). https://doi.org:10.1021/acsomega.2c01048

7 Tong, W. *et al.* Tributyl phosphate degradation and phosphorus immobilization by MnO2: Reaction condition optimization and mechanism exploration. *Journal of Hazardous Materials* **432**, 128725 (2022). https://doi.org:https://doi.org/10.1016/j.jhazmat.2022.128725

8 Guo, X. *et al.* Self-accelerated corrosion of nuclear waste forms at material interfaces. *Nature Materials* **19**, 310-316 (2020). https://doi.org:10.1038/s41563-019-0579-x

9 Li, J., Li, L. & Jonsson, M. Formation and stability of studtite in bicarbonate-containing waters. *Ecotoxicology and Environmental Safety* **263**, 115297 (2023). https://doi.org:https://doi.org/10.1016/j.ecoenv.2023.115297

10 Guo, X. *et al.* Energetics of metastudtite and implications for nuclear waste alteration. *Proceedings of the National Academy of Sciences* **111**, 17737-17742 (2014). https://doi.org:doi:10.1073/pnas.1421144111

11 Kravchuk, D. V. *et al.* Isolation and Reactivity of Uranyl Superoxide. *Angewandte Chemie International Edition* **60**, 15041-15048 (2021). https://doi.org:https://doi.org/10.1002/anie.202103039

12 Odoh, S. O. *et al.* Structure and Reactivity of X-ray Amorphous Uranyl Peroxide, U2O7. *Inorganic Chemistry* **55**, 3541-3546 (2016). https://doi.org:10.1021/acs.inorgchem.6b00017

13 Abdel-Rahman, M. A. & El-Mongy, S. A. Ore leashing processing for yellow cake production and assay of their uranium content by radiometric analysis. *Zeitschrift für anorganische und allgemeine Chemie* **644**, 29-32 (2018).

14 Litz, J. & Coleman, R. A review of United States yellow cake precipitation practice. *Production of Yellow Cake and Uranium Fluorides* **101** (1979).

15 Hanson, B. D. *et al.* Corrosion of commercial spent nuclear fuel. 1. Formation of studtite and metastudtite. *Radiochimica Acta* **93**, 159-168 (2005). https://doi.org:doi:10.1524/ract.93.3.159.61613

16 Abbott, D. Limits to growth: Can nuclear power supply the world's needs? *Bulletin of the Atomic Scientists* **68**, 23-32 (2012). https://doi.org:10.1177/0096340212459124

17 Armstrong, C. R. *et al.* Uranyl peroxide enhanced nuclear fuel corrosion in seawater. *Proceedings of the National Academy of Sciences* **109**, 1874-1877 (2012). https://doi.org:doi:10.1073/pnas.1119758109

18 Stepanov, S. I. & Boyarintsev, A. V. Reprocessing of spent nuclear fuel in carbonate media: Problems, achievements, and prospects. *Nuclear Engineering and Technology* **54**, 2339-2358 (2022). https://doi.org:https://doi.org/10.1016/j.net.2022.01.009

19 Qiu, J. & Burns, P. C. Clusters of Actinides with Oxide, Peroxide, or Hydroxide Bridges. *Chemical Reviews* **113**, 1097-1120 (2013). https://doi.org:10.1021/cr300159x
20 Burns, P. C. & Nyman, M. Captivation with encapsulation: a dozen years of exploring uranyl peroxide capsules. *Dalton Transactions* **47**, 5916-5927 (2018). https://doi.org:10.1039/C7DT04245K
21 Dembowski, M. *et al.* Computationally-Guided Assignment of Unexpected Signals in the Raman Spectra of Uranyl Triperoxide Complexes. *Inorganic Chemistry* **56**, 1574-1580 (2017). https://doi.org:10.1021/acs.inorgchem.6b02666
22 Olander, D. Nuclear fuels – Present and future. *Journal of Nuclear Materials* **389**, 1-22 (2009). https://doi.org:https://doi.org/10.1016/j.jnucmat.2009.01.297
23 Bruno, J. & Ewing, R. C. Spent nuclear fuel. *Elements* **2**, 343-349 (2006).
24 Choppin, G., Liljenzin, J.-O., Rydberg, J. & Ekberg, C. *Radiochemistry and nuclear chemistry*. (Academic Press, 2013).
25 Knief, R. A. Nuclear engineering: theory and technology of commercial nuclear power. *(No Title)* (1992).
26 Vondy, D., Lane, J. & Gresky, A. Production of Np237 and Pu238 in thermal power reactors. *Industrial & Engineering Chemistry Process Design and Development* **3**, 293-296 (1964).
27 Burns, P. C. *et al.* Actinyl Peroxide Nanospheres. *Angewandte Chemie International Edition* **44**, 2135-2139 (2005). https://doi.org:https://doi.org/10.1002/anie.200462445
28 Clark, D. L. *et al.* Chemical Speciation of Neptunium(VI) under Strongly Alkaline Conditions. Structure, Composition, and Oxo Ligand Exchange. *Inorganic Chemistry* **52**, 3547-3555 (2013). https://doi.org:10.1021/ic3020139
29 Hickam, S. *et al.* Neptunyl Peroxide Chemistry: Synthesis and Spectroscopic Characterization of a Neptunyl Triperoxide Compound, Ca2[NpO2(O2)3]·9H2O. *Inorganic Chemistry* **58**, 12264-12271 (2019). https://doi.org:10.1021/acs.inorgchem.9b01712
30 Forbes, T., Kruse, S., Scherrer, S. K., Holmbeck, G. P. & Laverne, J. A. The Inorganic Chemist's Guide to Actinide Radiation Chemistry: A Review. *Inorganic Chemistry Frontiers* (2025). https://doi.org:10.1039/D5QI00975H
31 Nyman, M., Rodriguez, M. A. & Campana, C. F. Self-Assembly of Alkali-Uranyl-Peroxide Clusters. *Inorganic Chemistry* **49**, 7748-7755 (2010). https://doi.org:10.1021/ic1005192
32 Hutchison, D. C. *et al.* Synthesis of Single Crystal Li2NpO4 and Li4NpO5 from Aqueous Lithium Hydroxide Solutions under Mild Hydrothermal Conditions. *Inorganic Chemistry* **62**, 16564-16573 (2023). https://doi.org:10.1021/acs.inorgchem.3c02460
33 Fortier, S. & Hayton, T. W. Oxo ligand functionalization in the uranyl ion (UO22+). *Coordination Chemistry Reviews* **254**, 197-214 (2010). https://doi.org:https://doi.org/10.1016/j.ccr.2009.06.003
34 Bjorklund, J. L., Pyrch, M. M., Basile, M. C., Mason, S. E. & Forbes, T. Z. Actinyl-cation interactions: experimental and theoretical assessment of [Np(vi)O2Cl4]2− and [U(vi)O2Cl4]2− systems. *Dalton Transactions* **48**, 8861-8871 (2019). https://doi.org:10.1039/c9dt01753d
35 Danis, J. A., Lin, M. R., Scott, B. L., Eichhorn, B. W. & Runde, W. H. Coordination Trends in Alkali Metal Crown Ether Uranyl Halide Complexes: The Series

[A(Crown)]2[UO2X4] Where A = Li, Na, K and X = Cl, Br. *Inorganic Chemistry* **40**, 3389-3394 (2001). https://doi.org:10.1021/ic0011056

36 Lu, G., Forbes, T. Z. & Haes, A. J. Evaluating Best Practices in Raman Spectral Analysis for Uranium Speciation and Relative Abundance in Aqueous Solutions. *Analytical Chemistry* **88**, 773-780 (2016). https://doi.org:10.1021/acs.analchem.5b03038

37 Lu, G., Haes, A. J. & Forbes, T. Z. Detection and identification of solids, surfaces, and solutions of uranium using vibrational spectroscopy. *Coordination chemistry reviews* **374**, 314-344 (2018). https://doi.org:10.1016/j.ccr.2018.07.010

38 Rajapaksha, H., Mason, S. E., Augustine, L. J. & Forbes, T. Guiding Principles for the Rational Design of Hybrid Materials: Use of DFT Methodology for Evaluating Non-Covalent Interactions in a Uranyl Tetrahalide Model System. *Angewandte Chemie International Edition* **135**, e202305073 (2023). https://doi.org:https://doi.org/10.1002/anie.202305073

39 Rajapaksha, H. *et al.* Three-Dimensional Noncovalent Interaction Network within [NpO2Cl4]2– Coordination Compounds: Influence on Thermochemical and Vibrational Properties. *Inorganic Chemistry* **62**, 17265–17275 (2023). https://doi.org:10.1021/acs.inorgchem.3c02502

40 Clark, D. L. *et al.* Chemical Speciation of the Uranyl Ion under Highly Alkaline Conditions. Synthesis, Structures, and Oxo Ligand Exchange Dynamics. *Inorganic Chemistry* **38**, 1456-1466 (1999). https://doi.org:10.1021/ic981137h

41 Margate, J. *et al.* Chronicles of plutonium peroxides: spectroscopic characterization of a new peroxo compound of Pu(iv). *Chemical Communications* **60**, 6260-6263 (2024). https://doi.org:10.1039/D4CC01186D

42 Pyrch, M. M. *et al.* Impacts of hydrogen bonding interactions with Np(v/vi)O2Cl4 complexes: vibrational spectroscopy, redox behavior, and computational analysis. *Dalton Transactions* **49**, 6854-6866 (2020). https://doi.org:10.1039/d0dt00848f

43 Pyrch, M. M., Augustine, L. J., Williams, J. M., Mason, S. E. & Forbes, T. Z. Use of vibrational spectroscopy to identify the formation of neptunyl–neptunyl interactions: a paired density functional theory and Raman spectroscopy study. *Dalton Transactions* **51**, 4772-4785 (2022). https://doi.org:10.1039/D2DT00200K

44 Grimme, S. Accurate Calculation of the Heats of Formation for Large Main Group Compounds with Spin-Component Scaled MP2 Methods. *The Journal of Physical Chemistry A* **109**, 3067-3077 (2005). https://doi.org:10.1021/jp050036j

45 Wittmann, L., Neugebauer, H., Grimme, S. & Bursch, M. Dispersion-corrected r2SCAN based double-hybrid functionals. *The Journal of Chemical Physics* **159** (2023). https://doi.org:10.1063/5.0174988

46 Tao, J., Perdew, J. P., Staroverov, V. N. & Scuseria, G. E. Climbing the Density Functional Ladder: Nonempirical Meta--Generalized Gradient Approximation Designed for Molecules and Solids. *Physical Review Letters* **91**, 146401 (2003). https://doi.org:10.1103/PhysRevLett.91.146401

47 Hammer, B., Hansen, L. B. & Nørskov, J. K. Improved adsorption energetics within density-functional theory using revised Perdew-Burke-Ernzerhof functionals. *Physical Review B* **59**, 7413-7421 (1999). https://doi.org:10.1103/PhysRevB.59.7413

48 Kovács, A., Konings, R. J. M., Gibson, J. K., Infante, I. & Gagliardi, L. Quantum Chemical Calculations and Experimental Investigations of Molecular Actinide Oxides. *Chemical Reviews* **115**, 1725-1759 (2015). https://doi.org:10.1021/cr500426s

49 Bader, R. F. W. A quantum theory of molecular structure and its applications. *Chemical Reviews* **91**, 893-928 (1991). https://doi.org:10.1021/cr00005a013

50 Scherrer, S. K., Rajapaksha, H., Kravchuk, D. V., Mason, S. E. & Forbes, T. Z. Impacts of trace level chromium on formation of superoxide within uranyl triperoxide complexes. *Chemical Communications* **60**, 10584-10587 (2024). https://doi.org:10.1039/D4CC03194F

51 Scherrer, S. K. *et al.* Superoxide Radicals in Uranyl Peroxide Solids: Lasting Signatures Identified by Electron Paramagnetic Resonance Spectroscopy. *Angewandte Chemie International Edition* **63**, e202400379 (2024). https://doi.org:https://doi.org/10.1002/anie.202400379

52 Che, M. & Sojka, Z. Electron transfer processes at the surface of MoOx/SiO2 catalysts. *Topics in Catalysis* **15**, 211-217 (2001). https://doi.org:10.1023/A:1016601815952

53 Sobańska, K. *et al.* Diagnostic Features of EPR Spectra of Superoxide Intermediates on Catalytic Surfaces and Molecular Interpretation of Their g and A Tensors. *Topics in Catalysis* **58**, 796-810 (2015). https://doi.org:10.1007/s11244-015-0420-y

54 Pietrzyk, P., Podolska, K., Mazur, T. & Sojka, Z. Heterogeneous Binding of Dioxygen: EPR and DFT Evidence for Side-On Nickel(II)–Superoxo Adduct with Unprecedented Magnetic Structure Hosted in MFI Zeolite. *Journal of the American Chemical Society* **133**, 19931-19943 (2011). https://doi.org:10.1021/ja208387q

55 Dietzel, P. D. C., Kremer, R. K. & Jansen, M. Tetraorganylammonium Superoxide Compounds: Close to Unperturbed Superoxide Ions in the Solid State. *Journal of the American Chemical Society* **126**, 4689-4696 (2004). https://doi.org:10.1021/ja039880i

56 Odom, B., Hanneke, D., D'Urso, B. & Gabrielse, G. New Measurement of the Electron Magnetic Moment Using a One-Electron Quantum Cyclotron. *Physical Review Letters* **97**, 030801 (2006). https://doi.org:10.1103/PhysRevLett.97.030801

57 Schreckenbach, G. & Ziegler, T. Calculation of the G-Tensor of Electron Paramagnetic Resonance Spectroscopy Using Gauge-Including Atomic Orbitals and Density Functional Theory. *The Journal of Physical Chemistry A* **101**, 3388-3399 (1997). https://doi.org:10.1021/jp963060t

58 Weil, J. A. & Bolton, J. R. *Electron Paramagnetic Resonance: Elementary Theory and Practical Applications*. (Wiley, 2007).

59 Owenius, R., Engström, M., Lindgren, M. & Huber, M. Influence of Solvent Polarity and Hydrogen Bonding on the EPR Parameters of a Nitroxide Spin Label Studied by 9-GHz and 95-GHz EPR Spectroscopy and DFT Calculations. *The Journal of Physical Chemistry A* **105**, 10967-10977 (2001). https://doi.org:10.1021/jp0116914

60 Engström, M., Owenius, R. & Vahtras, O. Ab initio g-tensor calculations of hydrogen bond effects on a nitroxide spin label. *Chemical Physics Letters* **338**, 407-413 (2001). https://doi.org:https://doi.org/10.1016/S0009-2614(01)00311-6

61 Fukuzumi, S. & Ohkubo, K. Quantitative Evaluation of Lewis Acidity of Metal Ions Derived from the g Values of ESR Spectra of Superoxide: Metal Ion Complexes in Relation to the Promoting Effects in Electron Transfer Reactions. *Chemistry – A European Journal* **6**, 4532-4535 (2000). https://doi.org:https://doi.org/10.1002/1521-3765(20001215)6:24<4532::AID-CHEM4532>3.0.CO;2-9

62 Kruse, S. J., Rajapaksha, H., LaVerne, J. A., Mason, S. E. & Forbes, T. Z. Radiation-Induced Defects in Uranyl Trinitrate Solids. *Chemistry – A European Journal* **30**, e202400956 (2024). https://doi.org:https://doi.org/10.1002/chem.202400956

63 Zaichenko, A., Schröder, D., Janek, J. & Mollenhauer, D. Pathways to Triplet or Singlet Oxygen during the Dissociation of Alkali Metal Superoxides: Insights by Multireference Calculations of Molecular Model Systems. *Chemistry – A European Journal* **26**, 2395-2404 (2020). https://doi.org:https://doi.org/10.1002/chem.201904110

64 Gendron, F. *et al.* Magnetic Properties and Electronic Structure of Neptunyl(VI) Complexes: Wavefunctions, Orbitals, and Crystal-Field Models. *Chemistry – A European Journal* **20**, 7994-8011 (2014). https://doi.org:https://doi.org/10.1002/chem.201305039

65 Wedal, J. C., Moore, W. N. G., Lukens, W. W. & Evans, W. J. Perplexing EPR Signals from 5f36d1 U(II) Complexes. *Inorganic Chemistry* **63**, 2945-2953 (2024). https://doi.org:10.1021/acs.inorgchem.3c03449

66 Wolford, N. J., Yu, X., Bart, S. C., Autschbach, J. & Neidig, M. L. Ligand effects on electronic structure and bonding in U(iii) coordination complexes: a combined MCD, EPR and computational study. *Dalton Transactions* **49**, 14401-14410 (2020). https://doi.org:10.1039/D0DT02929G

67 Gaiser, A. N. *et al.* Creation of an unexpected plane of enhanced covalency in cerium(III) and berkelium(III) terpyridyl complexes. *Nature Communications* **12**, 7230 (2021). https://doi.org:10.1038/s41467-021-27576-y

68 Nienhuis, E. T. *et al.* Cations impact radical reaction dynamics in concentrated multicomponent aqueous solutions. *The Journal of Chemical Physics* **158** (2023). https://doi.org:10.1063/5.0153132

69 Misak, A. *et al.* EPR Study of KO2 as a Source of Superoxide and •BMPO-OH/OOH Radical That Cleaves Plasmid DNA and Detects Radical Interaction with H2S and Se-Derivatives. *Antioxidants* **10**, 1286 (2021).

70 Misak, A. *et al.* •BMPO-OOH Spin-Adduct as a Model for Study of Decomposition of Organic Hydroperoxides and the Effects of Sulfide/Selenite Derivatives. An EPR Spin-Trapping Approach. *Antioxidants* **9**, 918 (2020).

71 Zhao, H., Joseph, J., Zhang, H., Karoui, H. & Kalyanaraman, B. Synthesis and biochemical applications of a solid cyclic nitrone spin trap: a relatively superior trap for detecting superoxide anions and glutathiyl radicals. *Free Radical Biology and Medicine* **31**, 599-606 (2001).

72 Bézière, N. *et al.* Metabolic stability of superoxide adducts derived from newly developed cyclic nitrone spin traps. *Free Radical Biology and Medicine* **67**, 150-158 (2014).

73 Suzen, S., Gurer-Orhan, H. & Saso, L. Detection of reactive oxygen and nitrogen species by electron paramagnetic resonance (EPR) technique. *Molecules* **22**, 181 (2017).

74 Eaton, S. S., Eaton, G. R. & Berliner, L. J. *Biomedical EPR-Part A: Free radicals, metals, medicine and physiology*. (Springer Science & Business Media, 2004).

75 Buettner, G. R. Spin trapping: ESR parameters of spin adducts. *Free Radic Biol Med* **3**, 259-303 (1987). https://doi.org:10.1016/s0891-5849(87)80033-3

76 Finkelstein, E., Rosen, G. M. & Rauckman, E. J. Spin trapping of superoxide and hydroxyl radical: Practical aspects. *Archives of Biochemistry and Biophysics* **200**, 1-16 (1980). https://doi.org:https://doi.org/10.1016/0003-9861(80)90323-9

77 Tsai, P., Marra, J. M., Pou, S., Bowman, M. K. & Rosen, G. M. Is there stereoselectivity in spin trapping superoxide by 5-tert-butoxycarbonyl-5-methyl-1-pyrroline N-oxide? *The Journal of Organic Chemistry* **70**, 7093-7097 (2005).

78 Tsai, P. *et al.* Esters of 5-carboxyl-5-methyl-1-pyrroline N-oxide: a family of spin traps for superoxide. *The Journal of organic chemistry* **68**, 7811-7817 (2003).

Table of contents

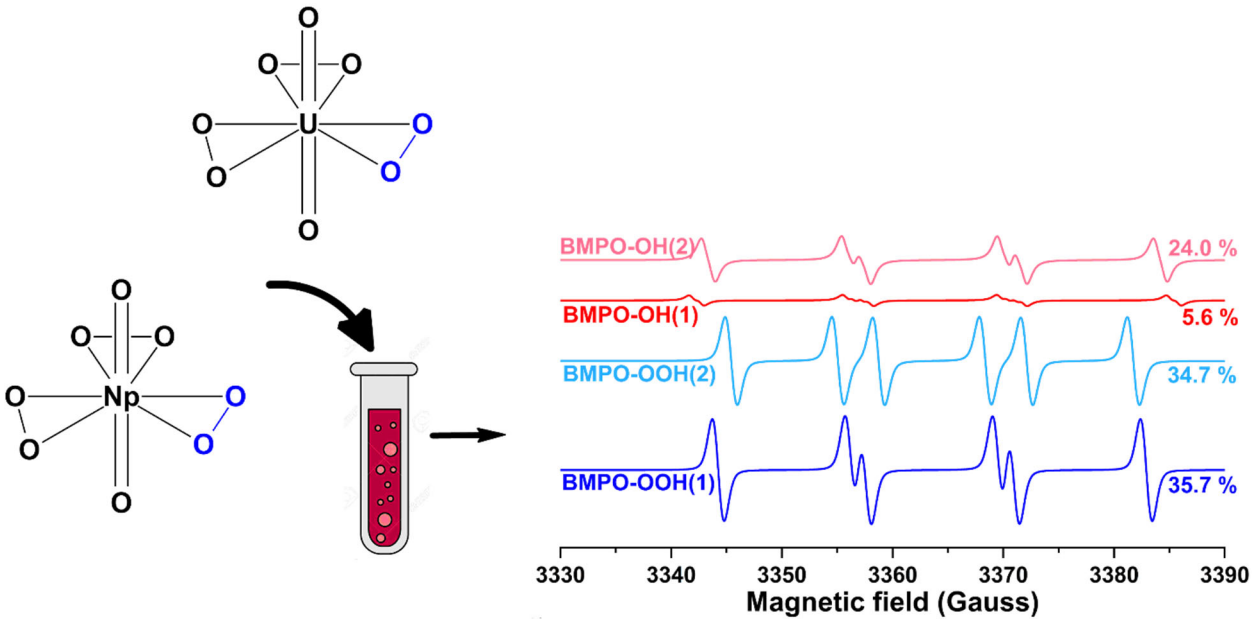

Uranyl and neptunyl superoxide complexes were detected through EPR spectroscopy with spin-traps